Contrails and Their Impact on Shortwave Radiation and Photovoltaic Power Production - A Regional Model Study

Simon Gruber[1], Simon Unterstrasser[2], Jan Bechtold[3], Heike Vogel[1], Bernhard Vogel[1], Martin Jung[3], and Henry Pak[3]

[1]Karlsruhe Institute of Technology – Institute of Meteorology and Climate Research, Hermann-von-Helmholtz-Platz 1, 76344 Eggenstein-Leopoldshafen, Germany
[2]Deutsches Zentrum für Luft- und Raumfahrt (DLR) – Institut für Physik der Atmosphäre, Oberpfaffenhofen, 82234 Wessling, Germany
[3]Deutsches Zentrum für Luft- und Raumfahrt (DLR) – Institut für Flughafenwesen und Luftverkehr, 51147 Cologne, Germany

Correspondence to: S. Gruber (simon.gruber@kit.edu)

Abstract. A high resolution regional-scale numerical model was extended by a parameterization that allows for both the generation and the life cycle of contrails and contrail cirrus to be calculated. The life cycle of contrails and contrail cirrus is described by a two-moment cloud microphysical scheme that was extended by a separate contrail ice class for a better representation of the high concentration of small ice crystals that occur in contrails. The basic input data set contains the spatially and
5 temporally highly resolved flight trajectories over Central Europe derived from real time data. The parameterization provides aircraft-dependent source terms for contrail ice mass and number. A case study was performed to investigate the influence of contrails and contrail cirrus on the radiative fluxes at the earth's surface. Accounting for contrails produced by aircraft enabled the model to simulate high clouds that were otherwise missing on this day. The effect of these extra clouds was to reduce the incoming shortwave radiation at the surface as well as the production of photovoltaic power by up to 10 %.

10 ## 1 Introduction

Contrails consist of ice crystals formed in the exhaust plume of aircraft due to a mixing of the hot exhaust with cold environmental air. Following the Schmidt-Appleman-Criterion (Schmidt, 1941; Appleman, 1953; Schumann, 1996), contrails form only when the ambient temperature is below a threshold temperature of roughly $-45°$ C. With a favorable state of the atmosphere, i.e. characterized by supersaturation with respect to ice, the originally line-shaped contrails undergo various physical processes
15 at the micro scale, spread by the influence of shear and sedimentation and change their structure and microphysical properties. At some point, contrails are no longer distinguishable from natural cirrus in observations. This type of anthropogenic cloud is then called contrail cirrus (Heymsfield et al., 2010) and can have lifetimes of several hours. In a particular case, an 18-hour old contrail-cirrus could be tracked in a satellite imagery (Minnis et al., 1998).

Contrails influence the radiative budget of the atmosphere in a way that is comparable to that of thin natural cirrus clouds
20 (Sausen et al., 2005). Important properties, such as the optical depth or the spatial and temporal extent of occurrence, have not been sufficiently investigated and are also not quantified to a satisfactory extent (Boucher et al., 2013). The radiative forcing of

aged contrails and contrail cirrus is of greater importance than the one originating from young, line-shaped contrails (Stubenrauch and Schumann, 2005; Eleftheratos et al., 2007; Burkhardt and Kärcher, 2011).

Previous model studies primarily used global circulation models extended by parameterizations that are able to simulate line-shaped contrails. Here, the global radiative forcing due to contrails was quantified. The values spread around 0.4 mWm^{-2}

5 (Ponater et al., 2002) to 3.5 mWm^{-2} (Marquart et al., 2003). Taking the larger effect of contrail cirrus into account, a global mean radiative forcing of approximately 38 mWm^{-2} (Burkhardt and Kärcher, 2011) to 40 to 80 mWm^{-2} (Schumann and Graf, 2013) is found. The major drawbacks of these methods are the coarse resolution of the models in both space and time.

Another class of studies simulates single contrails with high resolution LES[1] or RANS[2] models, hereby focusing on contrail formation (Paoli et al., 2013; Khou et al., 2015), young contrails with ages up to 5 minutes and their interaction with the

10 descending wake vortices (Lewellen and Lewellen, 2001; Unterstrasser, 2014) and the transition into contrail-cirrus over time scales of hours (Unterstrasser and Gierens, 2010a; Lewellen, 2014). Usually, the contrail evolution is studied for a variety of environmental scenarios which helps to single out important process and ambient and aircraft parameters. Parameter studies allow for investigating the conditions under which contrails are persistent and the manner in which microphysical and optical properties change during transition and decay. Because this method is not applicable for a larger number of contrails and often

15 limited to idealized environmental scenarios, it is not suited to quantify the impact of air traffic on the state of the atmosphere. The spatial scale applied in this study lies between those typically used for large-eddy simulations and global climate models. In this respect, the presented study is complementary to the aforementioned approaches and is, to our knowledge, the first study of its kind. We use the online coupled regional-scale model system COSMO-ART (Baldauf et al., 2011; Vogel et al., 2009). In this context, online coupled means that meteorology, chemistry and contrail-related processes are simulated in one model

20 at the same grid and one main time step for integration is used. For this study, the model is extended by introducing a new hydrometeor class for contrail ice crystals. The contrail initialization is based on a parametrization of early contrail properties by Unterstrasser (2016). The prognostic equations for contrail ice are similar to those of the natural cirrus cloud class. Despite their similar treatment in terms of model equations, the evolution of the two cloud types can be quite different, as their formation mechanisms are different.

25 Ice crystals in young contrails are considerably smaller than the ones that form in natural cirrus clouds and occur with substantially higher ice crystal number concentrations (Febvre et al., 2009; Schröder et al., 2000; Voigt et al., 2010). Therefore, the original microphysical scheme was extended by a new hydrometeor class that allows for a separate treatment of the small contrail ice crystals separate from natural ice. This approach allows for the investigation of contrail microphysical properties and their changes during the various stages of development represented in a regional atmospheric model. In contrast to other

30 studies using a two-moment microphysical scheme (Bock and Burkhardt, 2016), the presented model configuration uses no fractional cloud coverage and no prognostic equations for contrail geometric properties like volume or area which describe the contrail spreading on the subgrid scale. Compared to GCM parameterizations, this omission seems acceptable in a regional model, as the spatial resolution is much higher (horizontal grid size of 2.8 km versus 250 km in a GCM).

---

[1]Large-Eddy Simulation

[2]Reynolds-Averaged Navier Stokes

Regarding the contrail microphysics and the interaction with the meteorological situation, the entire procedure is online coupled, thus allowing feedback processes between contrails and natural clouds in contrast to other models on a comparable grid scale (Schumann, 2012). One of the key goals of this study is thus to quantify the influence of contrails and contrail cirrus on natural high-level cloudiness. Moreover, the radiative properties of contrails and their local influence on the shortwave radiative

5   fluxes at the surface are examined.

The model uses a diagnostic radiation scheme (Ritter and Geleyn, 1992). Because the description of shortwave optical properties for ice clouds is optimized for different naturally occurring crystal habits (Fu et al., 1998; Key et al., 2002), a separate treatment of contrail ice crystals is introduced here as well.

The presented model configuration serves to study microphysical evolution of contrails and contrail cirrus, their influence on

10   natural high-level cloudiness, and their impact on the radiative fluxes on a regional scale and short time periods. This gains importance, e.g., in predicting the energy yield from photovoltaic (PV) systems, because additional cloud cover due to contrails is not represented in operational weather forecasting.

Another feature of this study is the new and recently developed data set of real time flight tracks. Rather than statistical calculations for globally averaged fuel consumption, the basic data consist of real time-based flight trajectories (flightradar24.com,

15   2015).

In section 2, the modification of the microphysical scheme and the radiation scheme are described. Section 3 presents a description of the parameterization providing the source terms for contrail ice. In section 4, the results of a case study and comparison with satellite observations are presented.

2   Model Description

20   In the following, the parameterizations to calculate the microphysical properties of ice crystals and the modifications to represent contrails are presented.

In this study, the COSMO-ART model is coupled with a comprehensive two-moment microphysical scheme following Seifert and Beheng (2006). Until now, the scheme contained one cloud ice class (besides other hydrometeor types in warm and mixed-phase clouds) that describes ice crystals in high-level ice clouds. Because ice crystals in freshly formed contrails are

25   considerably smaller than those in natural cirrus, the basic microphysical processes in young contrails are treated in a separate, newly introduced *contrail ice class*. From now on, the original ice cloud class is called *cirrus ice class*. The separate treatment allows simulating local bi-modal size spectra.

Consequently, also in the radiation scheme, contrails are treated separately from the cirrus ice using the new contrail ice class. The applied radiation scheme is described in section 2.2.

30   Unless otherwise indicated, the parameterized processes for the new contrail ice class are the same as those used for the cirrus ice class.

Similar approaches with a separate contrail ice class using climate models with coarser grid size are described by Burkhardt and Kärcher (2009) and Bock and Burkhardt (2016).

2.1 The Contrail Ice Class

In this section, we first describe shortly the treatment of ice crystals in the cirrus ice class. Hereby, we mainly focus on those aspects that are relevant for understanding contrail-specific modifications in the contrail ice class explained later on. A longer description including various formulae is deferred to the appendix.

5   In each grid box, the ice mass distribution is assumed to follow a generalized Γ-distribution $f(m)$ (see Eq. A1). Prognostic equations are solved for the ice crystal number concentration n (zeroth moment of $f(m)$) and the ice crystal mass concentration q_i (first moment of $f(m)$). Written concisely, the prognostic equations for the moments M^k of order $k = 0$ or 1 (see Eq. A2 for a definition) read as

$$\frac{\partial M^k}{\partial t} + \nabla \cdot \left[\boldsymbol{u} M^k \right] - \nabla \left[K_h \nabla M^k \right] + \frac{\partial}{\partial z} \left[\overline{v}_{sed,k} M^k \right] = S^k, \tag{1}$$

10   where $\boldsymbol{u}$ is the grid scale mean wind, K_h is the turbulent diffusion coefficient and $\overline{v}_{sed,k}$ is the number or mass-weighted sedimentation velocity (see Eq. A7). S^k comprises all source and sink terms like nucleation, deposition/sublimation and aggregation.

   The deposition source term is derived from the growth equation of a single ice crystal which is integrated over the whole ice crystal mass spectrum.

15   The ice crystals have a hexagonal shape and the mass m of a single ice crystal is related to its size L via the mass-size relation

$$m = a_{\mathrm{geo}} L^{b_{\mathrm{geo}}} \tag{2}$$

For m in kg and L in m, the parameter values are $a_{\mathrm{geo,nat}} = 1.59$ and $b_{\mathrm{geo,nat}} = 2.56$ (A. Seifert, personal communication, June, 01, 2017). In order to avoid unreasonably small or large mean masses $\overline{m} = q_i/n$, a lower limit $m_{\min} = 10^{-12}$ kg and upper limit 20 $m_{\max} = 10^{-6}$ kg are introduced. If $\overline{m}$ lies outside the interval $[m_{\min}, m_{\max}]$ in a grid box, the ice crystal number concentration is increased to $q_i/m_{\min}$ or reduced to $q_i/m_{\max}$, respectively. The limits correspond to sizes $L_{\min} = 17.5$ μm and $L_{\max} = 3800$ μm.

   The treatment of contrail ice is analogous to that of natural cirrus with only a few modifications. For the contrail ice class, the nucleation is switched off in the contrail ice class. Instead, the generation of contrail ice depends on air traffic and the atmospheric state and is explained in section 3.1. As mentioned before, most ice crystals in contrails are smaller than in natural 25   cirrus. We use a smaller lower limit $m_{\min} = 10^{-15}$ kg and employ a different mass-size relation which guarantees reasonable aspect ratios for small ice crystals. For this, we use a piece-wise definition of a_{geo} and b_{geo} (Spichtinger and Gierens, 2009; Heymsfield and Iaquinta, 2000). For masses above $m_{\mathrm{split}} = 2.15 \times 10^{-13}$ kg (corresponds to $L_{\mathrm{split}} = 7.42$ μm), $a_{\mathrm{geo,con}} = 0.04142$ and $b_{\mathrm{geo,con}} = 2.2$ are used. For masses below m_{split}, $a_{\mathrm{geo,con}} = 526.1$ and $b_{\mathrm{geo,con}} = 3.0$ is prescribed which defines quasi-spherical hexagonal columns with aspect ratio 1 (see derivation in Spichtinger and Gierens, 2009). The upper limit is set to a 30   relatively small value of $m_{\max} = 2 \times 10^{-11}$ kg and the treatment of grid boxes with too large mean masses is different compared to the cirrus ice class. Instead of bounding n, the total ice crystal mass and number from such a grid box are transferred from

the contrail ice class to the cirrus ice class. This is reasonable, as contrails show distinct bi-modal size spectra with many small ice crystals with sizes around 10 μm and fewer large ice crystals in the fall streaks (Unterstrasser et al., 2016a; Lewellen et al., 2014). The contrail ice class contains predominantly small ice crystals and the cirrus ice class allows for larger ice crystals that may also stem from aged contrails or contrail fall streaks. Using the new mass-size relation, the limits for $\overline{m}$ correspond to size $L_{\min} = 1.24$ μm and $L_{\max} = 58$ μm. One drawback of this approach is that the anthropogenic contribution in the cirrus ice class cannot be directly determined. Instead, we analyze the differences in the cirrus ice class between simulations with and without air traffic. This indirect quantification of the aged contrail contribution could be circumvented by introducing further contrail ice classes and may be implemented in the future.

The sedimentation parameterization and other components are as in the cirrus ice class.

The introduction of a second ice cloud class leads to a more complex behavior as both ice cloud classes are coupled and interact with each other in several ways. They are directly coupled via the collection process (see appendix) and the mass transfer of large contrail ice crystals as described above. Moreover, they interact indirectly via the competition for the available water vapor and possibly via dynamical changes through diabatic processes.

For a first illustration of our approach, Fig. 1 shows average size distributions (ASD) of a simulation with and without air traffic. Each ASD is a superposition of local Γ-distributions. In this example, the contrails are at most 4 hours old. More details on the simulation setup follow in section 4.1. The solid blue line shows the contrail ice class which has a peak at sizes around 20 μm. A less pronounced maximum is located at about 2 μm. The contribution of aged contrails becomes apparent by comparing the two dashed lines. Those show the cirrus ice class ASDs of a simulation with air traffic (blue) and without air traffic (green). Apparently, the anthropogenic contribution is substantial, in particular in terms of total number. The ice crystals in aged contrails are on average smaller than in natural cirrus and the peak size of the SD is shifted to a smaller value.

2.2 The Radiation Scheme

The atmospheric radiative fluxes in the COSMO-ART model are calculated using the GRAALS (General Radiative Algorithm Adapted to Linear-type Solutions) radiation scheme (Ritter and Geleyn, 1992). The algorithm needs as several input quantities such as temperature, pressure thickness of the model layers, trace gas concentrations, as well as the cloud cover and the mass mixing ratio for each hydrometor class considered (Ritter and Geleyn, 1992).

To consider contrails and contrail cirrus in the radiative algorithm, we include a contrail ice cloud cover determined from the contrail and contrail cirrus ice mass mixing ratio. Grid cells, in which the contrail or contrail cirrus ice mass mixing ratio exceeds 10^{-7} kg kg^{-1}, are considered to be covered with contrails or contrail cirrus.

Within the radiative algorithm, optical properties of hydrometeors are calculated. These are the mass specific extinction coefficient, single scattering albedo, asymmetry factor and the forward peak of the phase function. For ice clouds, the parameterizations following Fu et al. (1998) and Key et al. (2002) are used. Because they are optimized for natural ice clouds, the scheme computes reliable values for effective radii r_e between 5 and 60 μm (Fu et al., 1998), whereas for ice crystal populations with radii smaller than 5 μm, the parameterization is not well defined. Ice crystals in young contrails often have effective radii smaller than 5 μm. To overcome this problem, we are using the parameterization of Fu et al. (1998) and Key et al. (2002),
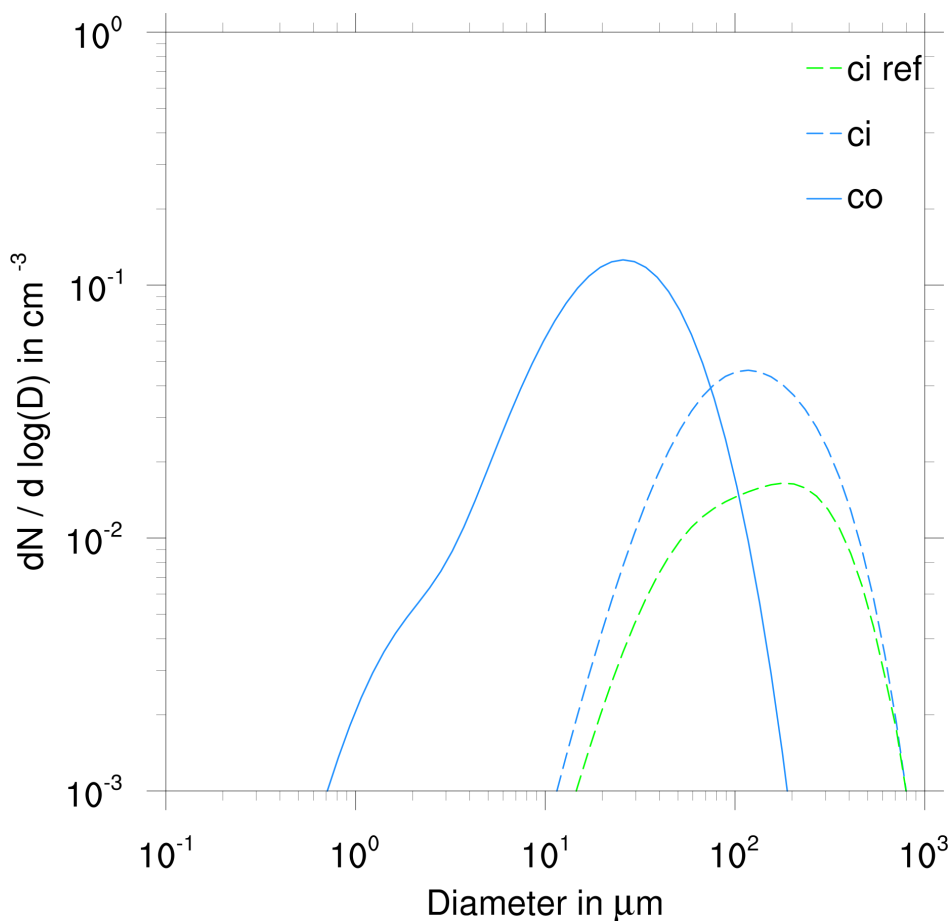
Figure 1. Ice crystal size distribution of the simulation with (blue) and without (green) aviation. For the simulation with aviation, separate ASDs of the contrail and cirrus cloud class are shown (solid and dotted line). 12 UTC.

but we prescribe a lower limit of $5\,\mu m$ for the calculation of the optical properties. For q_i, no limit is prescribed, instead, the simulated q_i is used to calculate the optical properties of the ice crystals. As the radiation scheme uses q_i and r_e for determining the radiative fluxes, implicitly fewer but larger crystals are assumed here. The extinction due to small ice crystals is expected to be larger than that for larger ones. Therefore, in our study, the radiative effect of young contrails may be underestimated.

5   The calculation of the contrail effective radii follows Fu et al. (1998). Here, the ice crystals are assumed to be randomly oriented, hexagonal columns.

$$r_e = \frac{1}{2}\left(\int_0^\infty D^2 L f_L\left(L\right)dL\right)\left(\int_0^\infty \left(DL + \frac{\sqrt{3}}{4}D^2\right)f_L\left(L\right)dL\right)^{-1} \tag{3}$$

D denotes the half width of an ice crystal which is implicitly given by the mass size relation (see Eq. B2). The size distribution f_L is related to the mass distribution $f(m)$ via the transformation property $f_L(L)dL = f(m(L))dm$. One can show that $f_L(L)$ (= number concentration per size range) follows a generalized Γ-distribution, if $f(m)$ (= number concentration per mass range) does so and the mass size relation is a potential function (see Eqs. B3 and B4).

3   Formation of Contrails

For the description of contrails, the first step is to check whether the environmental conditions are favorable for the formation of contrails. Here, the Schmidt-Appleman-Criterion (Schumann, 1996) is used which defines a threshold temperature below which contrail formation occurs.

10   In the second step, the source term of contrail ice mass and number has to be calculated. The parameterization used to calculate those source terms is described in detail in Unterstrasser (2016).

3.1   Initial Values for Contrails

Microphysical properties of contrails depend a lot more on the number of ice crystals than on the ice mass after the vortex phase (Unterstrasser and Gierens, 2010b). Therefore, it is appropriate to explicitly prescribe an initial ice crystal number con-

15   centration instead of an initial ice mass.

The presented procedure is applied at each model time step and for each grid cell, given that both an aircraft is present and the Schmidt-Appleman-Criterion is simultaneously fulfilled.

The parameterization provides ice crystal numbers for contrails that are about 5 minutes old. As meteorological input parameters, it requires the temperature T at cruise altitude, the ambient relative humidity with respect to ice RH_i and the Brunt-Väisälä

20   frequency N_{BV}. Furthermore, aircraft properties are characterized by the water vapor emission I_0, an 'emission' index for ice crystals EI_{iceno} and the wing span b_{span}.

We determine I_0 for medium fuel flow at cruise conditions as assumed in Unterstrasser and Görsch (2014). Here, a simple parabolic fit for I_0 depending on the wing span b_{span} is used (Unterstrasser, 2016). Information on the wing span is available in the flight track data (see section 3.2).

25   $$I_0 = c_1 \left(\frac{b_{span}}{c_2} \right)^2 ; \quad c_1 = 0.02 \text{ kg m}^{-1}; \quad c_2 = 80 \text{ m} \tag{4}$$

In this study only the most common JET-A fuel is assumed to be used; therefore EI_{iceno} is set to 2.8×10^{14} kg^{-1}.

The total number of ice crystals formed in the beginning, N_0, is calculated using the following equation:

$$N_0 = \frac{I_0}{EI_{\mathrm{H20}}} EI_{\mathrm{iceno}} \tag{5}$$

with water vapor emission index $EI_{\mathrm{H20}} = 1.25$. Note that EI_{iceno} is not reduced when the ambient temperature is only slightly below threshold temperature, even though in such situations fewer ice crystals would form (Kärcher et al., 2015).

The descending movement of the primary wake of an aircraft causes adiabatic heating within the plume. Due to this, sub-
5 limation and loss of ice crystals occurs, even in a supersaturated environment (e.g. Unterstrasser, 2016). As the spatial and temporal resolution of the model is too coarse to simulate these processes, the fraction of ice crystals surviving the vortex phase is parameterized by a loss factor λ_{Ns}. Details can be found in Unterstrasser (2016). The total number of surviving ice crystals per flight path N_{s} is calculated with:

$$N_{\mathrm{s}} = N_0 \lambda_{\mathrm{Ns}} \tag{6}$$

10 For the initial ice mass produced, the water vapor emission I_0 is used. The values for the produced ice mass and ice crystal number per flight distance are distributed equally on all grid cells, the aircraft passes within a time step:

$$n_{\mathrm{init}} = \frac{N_{\mathrm{s}} d}{V_{\mathrm{cell}}}; \quad q_{\mathrm{init}} = \frac{I_0 d}{V_{\mathrm{cell}}} \tag{7}$$

Here, V_{cell} denotes the volume of the grid cells, d is the flight distance within a grid box.

15 In global models, contrail parameterizations usually contain further prognostic equations that describe in some way the bulk contrail geometry (e.g. fractional cloud coverage or even some measure of contrail depth). In our approach, we assume that contrail ice crystals always populate the whole grid box as the horizontal scale is much smaller than in GCMs. In the vertical direction, it is reasonable to assume that ice crystals are distributed over the whole grid layer. In supersaturated conditions, contrail depth varies between 200 m and 600 m (mostly depending on aircraft type and stratification) and is similar to the
20 depth of the grid layer. In the horizontal plane, the simplifications could have a larger effect. If few flight routes transect a grid box and the segments are in total $d_{\mathrm{AT}} = 10$ km long then this implicitly results in an hypothetical initial contrail width of $\frac{2.8 \times 2.8}{10}$ km ≈ 800 m. This is larger than what is typically observed for 5 minute old contrails and better fits to 15 minute contrails (Freudenthaler et al., 1995). Hence, disregarding fractional coverage smears out the initialized contrails to some extent.
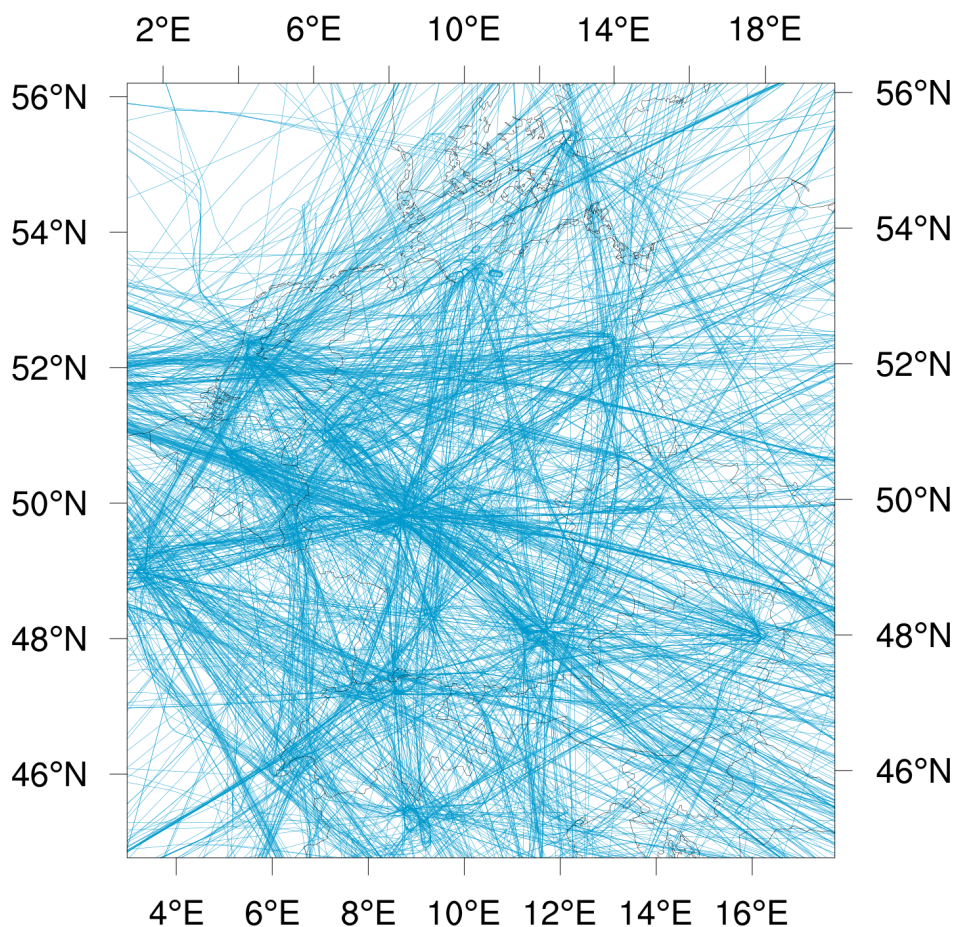
Figure 2. Flight trajectories for the COSMO-DE domain derived from ADS-B data (08 UTC - 16 UTC 3 December 2013). Each trajectory is plotted as a faint dashed line. Seemingly solid or thick lines are indicative of multiple overlaid trajectories.

3.2 Determination of Flight Tracks

In contrast to previously mentioned global modeling studies, this study uses a new and recently derived data set. Rather than statistical calculations for globally averaged fuel consumption, the basic data consist of exact flight trajectories over a limited area that are recorded from real time-based data (flightradar24.com, 2015). In addition to time, height and geographical position of the aircraft, information on aircraft type and current velocity is also available. In this study, besides position and time, we only use the wing span b_{span} as a proxy for the aircraft emission parameters (see section 3.1). The data set contains eight hours of air traffic, beginning at 08 UTC 3 December 2013 and ending at 16 UTC 3 December 2013. The trajectories of all flights during this period are displayed in Fig. 2.

4 Case Study

To test the methods described in the previous sections, a case study was performed. For this purpose, a situation over Germany with a high density of contrails in an otherwise cloud-free environment was chosen as the simulation period.

4.1 Model Setup

5 On 3 December 2013, the meteorological conditions over Central Europe were favorable for the formation of contrails. Additionally, the natural high-cloud coverage was relatively low, thus allowing for the identification of contrails on satellite images. For the case study, two simulations were conducted, both running for 24 hours, starting on 3 December 2013, 00 UTC. They use a horizontal 2.8×2.8 km grid and 60 vertical levels, resulting in a mean distance between the model layers of 300 m in the upper troposphere and 15 m in the lowest model layer. For boundary data, hourly COSMO re-analyses were used. In the

10 reference run, air traffic is turned off and the cirrus cloud class is the only ice cloud class to be active. For the run with air traffic, which we call aviation simulation, the previously explained configuration with two ice cloud classes is employed. Air traffic is switched on at 08 UTC and the two simulations evolve identically up to this point. Practically, a spin up phase shorter than 8 h could have been used, but from an operational point of view it was simpler to start the simulations at 00 UTC. As the data set of flight trajectories contains no information about air traffic after 16 UTC, no new contrails form after this time.

4.2 Simulated Contrail Properties

15 The contrail treatment in the microphysics scheme is designed such that contrail-induced changes occur both in the newly introduced contrail cloud class and in the existing cirrus cloud class. The contribution of young contrails can be directly assessed by evaluating the contrail cloud class. The contribution of aged contrails is found by comparing the cirrus cloud class of the aviation simulation and of the reference simulation.

20 Figure 3 shows ice cloud properties over Central Europe in the model layer centered at $z = 11900$ m, at 10 UTC. The various rows (from top to bottom) show the ice water content IWC, the ice crystal number concentration N, and the effective radius r_{e}. The left column shows the contrail cloud class of the aviation simulation, whereas the middle and right columns show the cirrus cloud class of the aviation and the reference simulation. At this time, contrails are at most two hours old and mostly consist of numerous very small ice crystals.

25 Independent of the considered quantity, the contrail cloud class features mostly line-shaped structures. The IWC reaches values up to 5 mg m^{-3}, which is larger than in the simulated natural cirrus. This hints at an accumulation of emitted water vapor additional to the ambient supersaturation. Furthermore, the absolute humidity at the heights considered is relatively low. Therefore, the IWC of natural cirrus is small and cirrus clouds are very thin and almost invisible. The ice crystal number concentrations often lie between 1 cm^{-3} and 100 cm^{-3} and can exceed those in natural cirrus by a factor of up to 1000.

30 Consequently, the ice crystal effective radii in contrails are much smaller and lie below 10 μm. The middle panel in Figure 4 shows that the most dense contrails over Northern Germany already leave a mark in the cirrus cloud class (see black box in panel b)). Notably, each line-shaped structure in the left panel corresponds to a pair of lines in the middle panel. This indicates
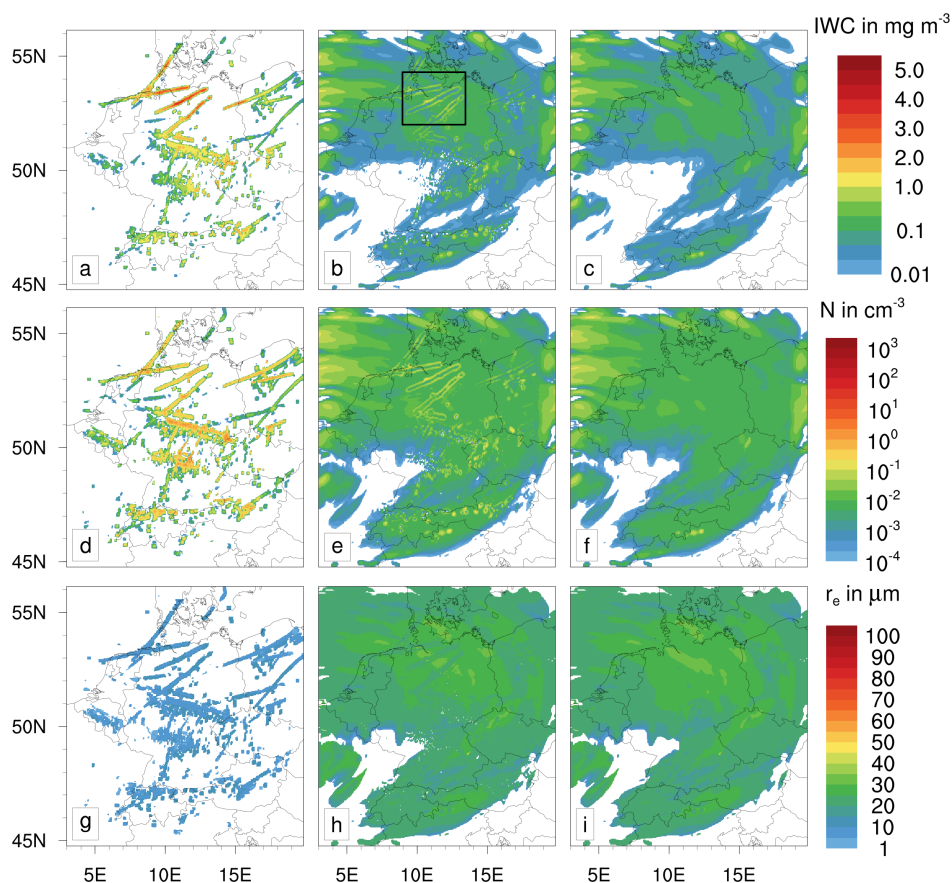
Figure 3. Various ice cloud properties are depicted for 10 UTC at an altitude of 11900 m (top row: ice water content; center row: ice crystal number concentration; bottom row: effective radii). Depicted are the simulation with aviation (left column: contrail class; middle column: cirrus cloud class) and without aviation (right column).

growth of ice crystals particularly at the margins where the contrail ice mass is soon transferred to the cirrus cloud class. Consistently, large-eddy simulation studies indicate the strongest growth at the edges of a contrail (Unterstrasser and Gierens, 2010a; Lewellen et al., 2014). A closer inspection (not shown) reveals that each line-shaped structure in the aforementioned box consists of several contrails. Those were produced by several aircraft that fly along the same route with short time sepa-

5 rations. Nevertheless, the IWC, N and r_e-values of the aged contrails and the surrounding natural cirrus shown in Fig. 3 are similar.

Figure 4 shows the situation at 12 UTC, analogous to Fig. 3 for 10 UTC. As time progresses, existing contrails continue to grow and further contrails are generated. Four hours after air traffic was activated in the model, a major part of the model layer is filled with contrails (left panel). Line-shaped patterns are still identifiable in some places, particularly over Northern

10 Germany. South of $52°$N many contrails overlap and represent a huge contrail cluster. Based on their visual appearance, no clear distinction from natural cirrus would be possible.
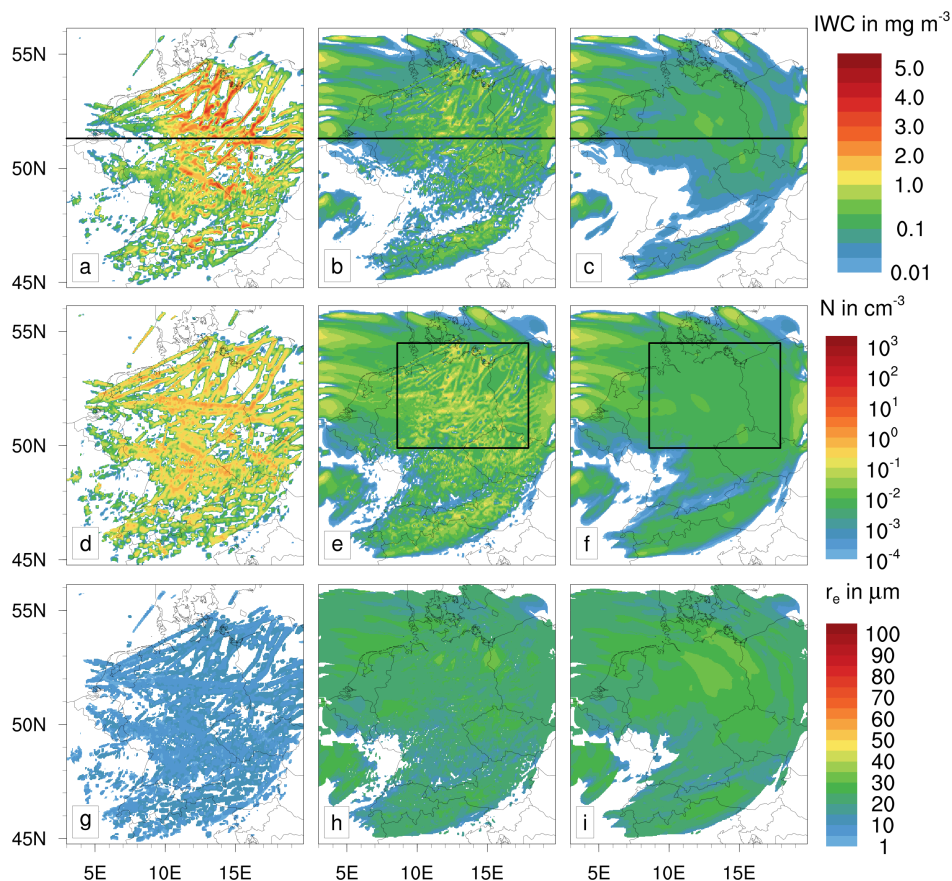
Figure 4. Analogous to Fig. 3, now for 12 UTC. The black horizontal lines indicate the location of the curtain displayed in Figs. 5 and 6; black boxes are discussed in the text.

Those contrail clusters still feature high IWC, high N, and low r_e values comparable to those two hours earlier and distinct to the surrounding natural cirrus. Moreover, we find lots of aged contrails over Germany (black box in middle panel), a region that is basically cirrus-free if there is no air traffic (black box in right panel). Again, the properties of the aged contrails and the natural cirrus around Germany are similar.

5 The results indicate that, in observations, microphysical criteria may help to separate at least young contrails from natural cirrus. In general, contrail fall streaks and aged contrails can not be identified as such once their linear shape is lost or masked. Unterstrasser et al. (2016b) shows that natural cirrus that forms in high-updraft scenarios can have ice crystal numbers similar to those of young contrails, which renders even the separation between young contrails and natural cirrus impossible. Moreover, they show that contrails that become embedded in natural cirrus have large volumes where ice crystals of both origin

10 co-exist. Hence, it is no longer meaningful to try to draw a strict separation line between natural cirrus and the anthropogenic cloud contribution.

Next, we analyze vertical distributions along the black line depicted in Fig. 4. Fig. 5 displays the relative humidity RH_i and
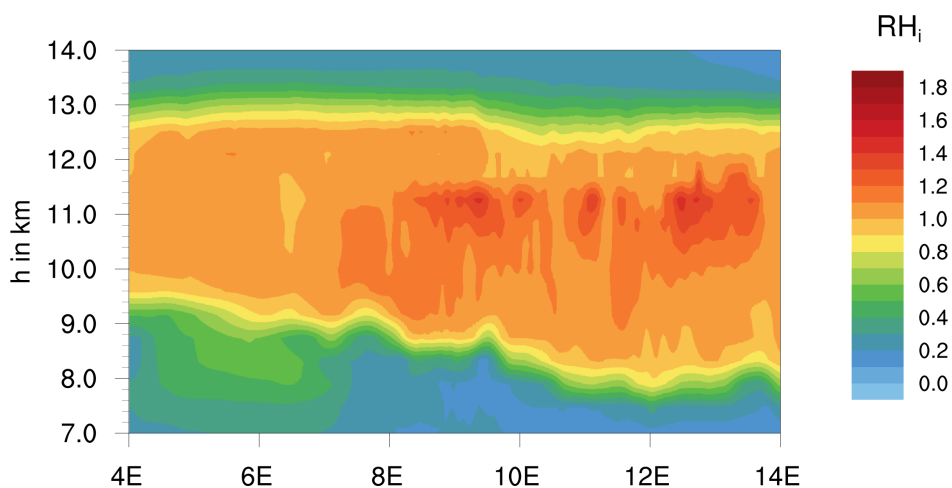
Figure 5. Vertical cross section of relative humidity RH_i at 12 UTC along the black line in Fig. 4.
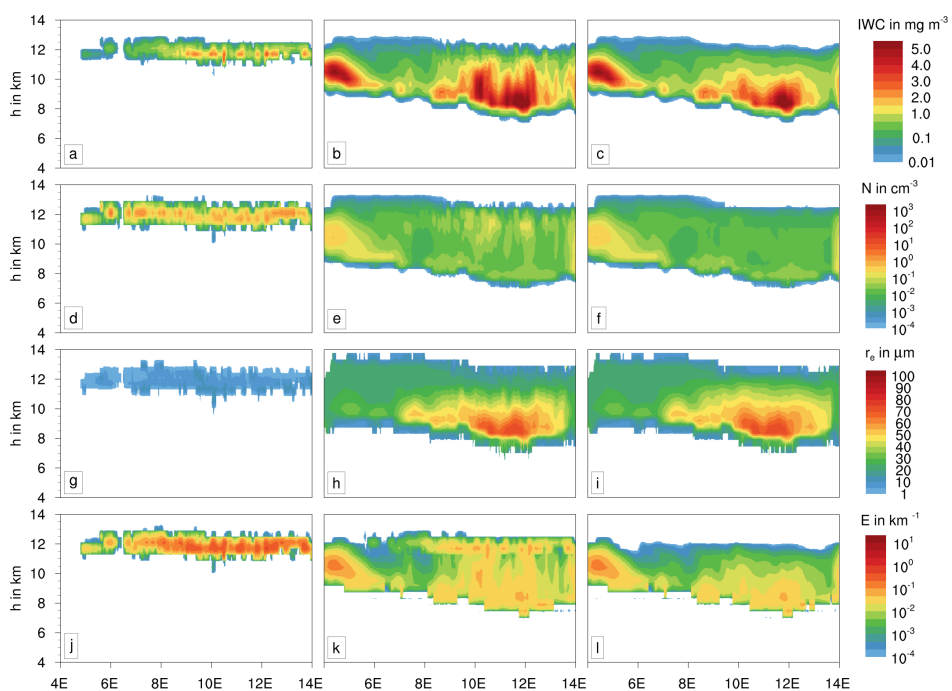
Figure 6. Vertical cross section of various contrail properties at 12 UTC along the black line in Fig. 4: ice water content, ice crystal number concentration, effective radius, and extinction coefficient (from top to bottom). Depicted are the simulation with aviation (left column: contrail class; middle column: cirrus cloud class) and without aviation (right column).
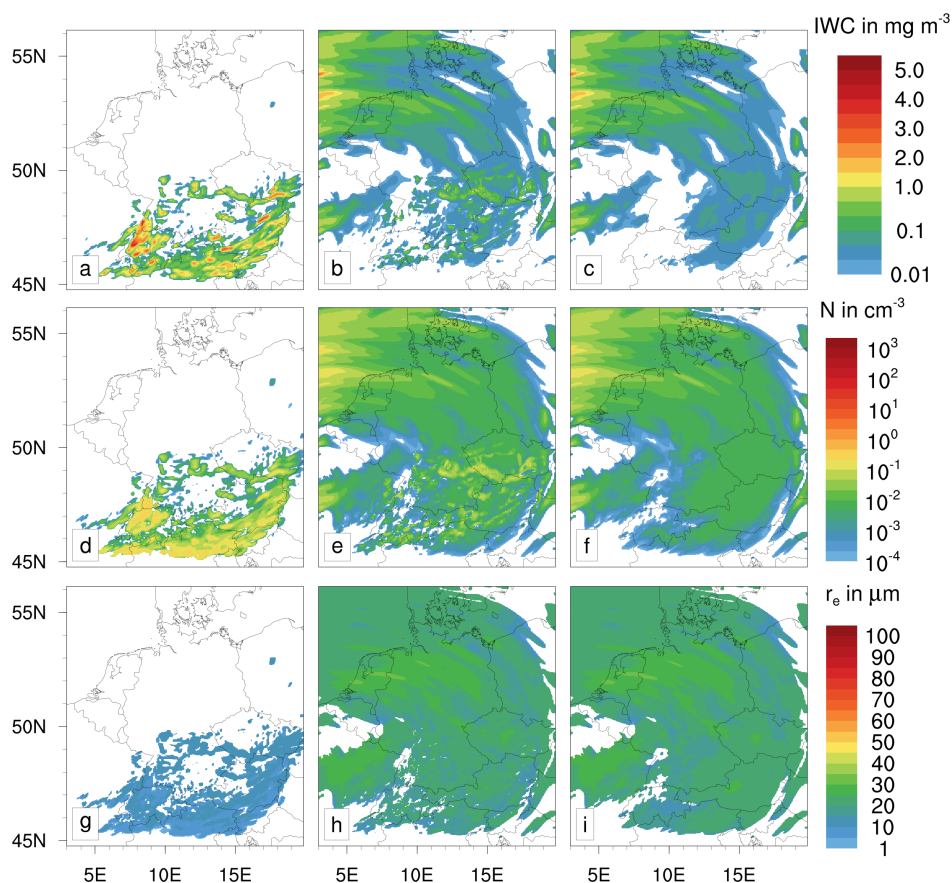
Figure 7. Analogous to Fig. 3, now for 20 UTC

reveals a remarkably thick layer with strong supersaturation that extends over the complete east-west extent of the model domain. The layer depth increases from 2.5 km in the west to more than 4 km in the east. These are generally very favorable conditions for the persistence and spreading of contrails.

Figure 6 shows the same ice cloud properties as Fig. 4 and additionally the extinction coefficient E at a wavelength of $1.115\,\mu$m.

5   Again, the left column shows the contrail cloud class of the aviation simulation, whereas the middle and right column show the cirrus cloud class of the aviation and the reference simulation.

In the reference simulation, natural ice is present over the entire supersaturated area. The number concentrations are mostly small, leading to optically thin cirrus clouds with extinction coefficients hardly exceeding 10^{-2} to 10^{-1} km^{-1}. Rather large ice crystals are present throughout the supersaturated area, with the largest values of r_e found in the lower part of the cirrus around

10   10 to $14°$ E.

In the aviation simulation, it becomes obvious from the left column plots that contrails form only at altitudes between 11 km and 13 km. As already seen in Fig. 4a;b, the IWC is comparable to that of natural cirrus, whereas number concentration reach

much higher values. The effective radii in the aviation simulation are typically one order of magnitude smaller than in natural cirrus clouds and do not exceed $10\,\mu m$. These results are in reasonable agreement with large-eddy studies (Unterstrasser and Gierens, 2010a; Lewellen et al., 2014). The numerous small crystals lead to high values for the extinction coefficient (up to $2\,\mathrm{km}^{-1}$). Therefore, contrail ice is of great importance for the radiation budget.

5   In the aviation simulation, changes in the natural ice class can be found mainly at heights where contrails form and slightly beyond. Here, local increases in IWC and N occur. Keeping in mind the simple design of our model setup, those ice crystals represent both fall streaks of contrails as well as the transition into contrail cirrus. In both processes, crystals number concentrations tend to decrease. In contrast, only a slight increase in r_e is found. In areas where contrail ice enters the cirrus class, a large increase in extinction coefficient occurs. Values of the extinction coefficient are comparable to those for the contrail ice
10   class and reach up to $1\,\mathrm{km}^{-1}$.

After 16 UTC, no new contrails are formed in our simulation. Four hours after the end of new contrail formation, the remaining contrail ice has been advected to the southern part of domain (Fig. 7). Local patterns of increased number concentrations in the cirrus ice class are now limited to those regions, where contrail ice is still present. The line shaped structures in the contrail ice class vanish, but relatively small values for r_e are still found throughout the domain.

15   In the northern part of domain, the cirrus ice class is again undisturbed by aviation. Here, no remarkable differences to the reference simulation can be seen. Obviously, including contrails in our model is not able to change the properties of natural cloud ice in an extensively temporal manner.

4.3   Comparison with Satellite Observation

With the exception of a cloud bank over the North and Baltic Seas and fog over Southern and Western Germany, a considerable
20   number of line-shaped contrails and diffuse cirrus clouds are present across the visible satellite image of 3 December 2013 at 12 UTC (Fig. 8a). A main contrail cluster is found over Central Germany. Contrails can also be identified over the Netherlands and Belgium, over the Czech Republic, and south of the Alps.

Figure 9 shows the CM SAF (EUMETSAT's Satellite Application Facility on Climate Monitoring) (Schulz et al., 2009) cloud types product CTY for 3 December 2013, 12 UTC. For simplification, the original types are grouped into low (l), medium
25   (m), high opaque (h,op) and high transparent (h,tr) clouds. In comparison with Fig. 8a, it seems likely that large parts of the transparent high-level clouds, especially over the center and the east of the domain (black box), consist of line shaped contrails and contrail cirrus.

The pattern of optical depth from the reference run (Fig. 8c) misses parts of the high-level transparent clouds over France and the south-eastern part of the domain in Fig. 9. These gaps are closed when contrails and contrail cirrus are included in the
30   simulation (black box in Fig. 8b). Over these areas, the simulation including aviation produces additional clouds, seen in the patterns of increased values for optical depth at $1.115\,\mu m$ (Fig. 8b). Mostly over the center of the domain, areas with values of τ between 0.2 to 0.6 and peaks up to 1.0 are simulated. This is in good agreement with the very high values of the extinction coefficient of contrails compared to those of natural cirrus (Fig. 6j, Fig. 6k, Fig. 6l). The line shaped patterns stem from the contrail ice class, the more patchy structures are due to aged contrails and the contrail cirrus that has been transformed to the
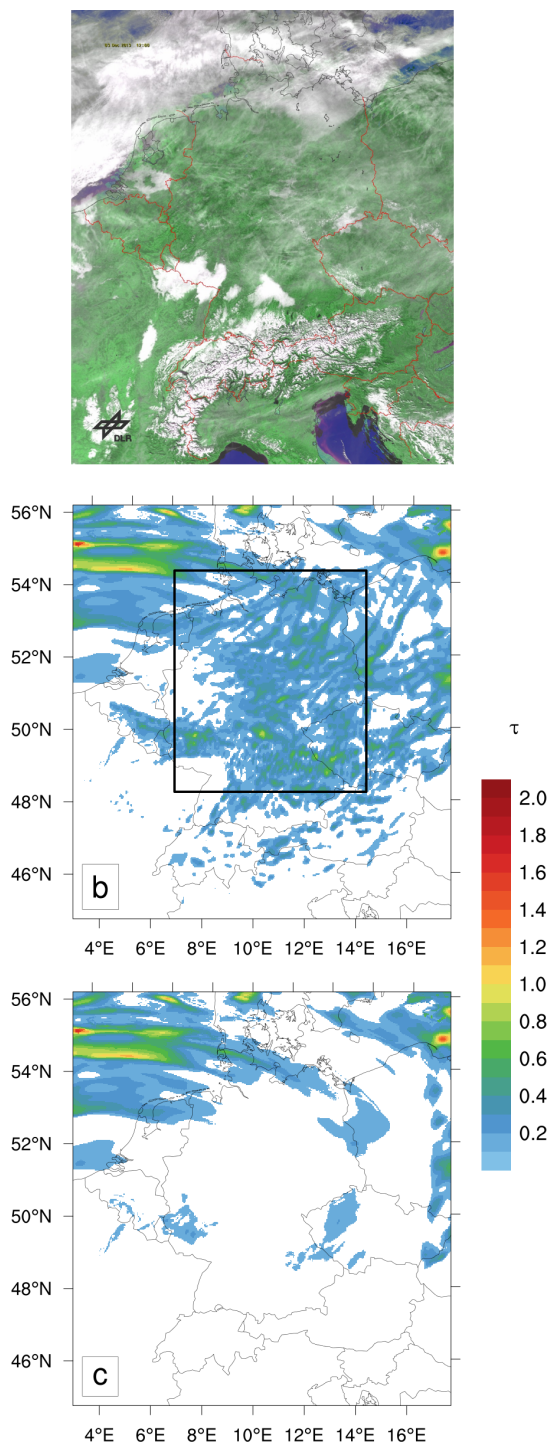
Figure 8. Contrails at 12 UTC: a) Satellite image (VIS) (DLR, 2014); b,c) optical depth of all ice clouds for the aviation simulation and the reference simulation. The black box is discussed in the text.
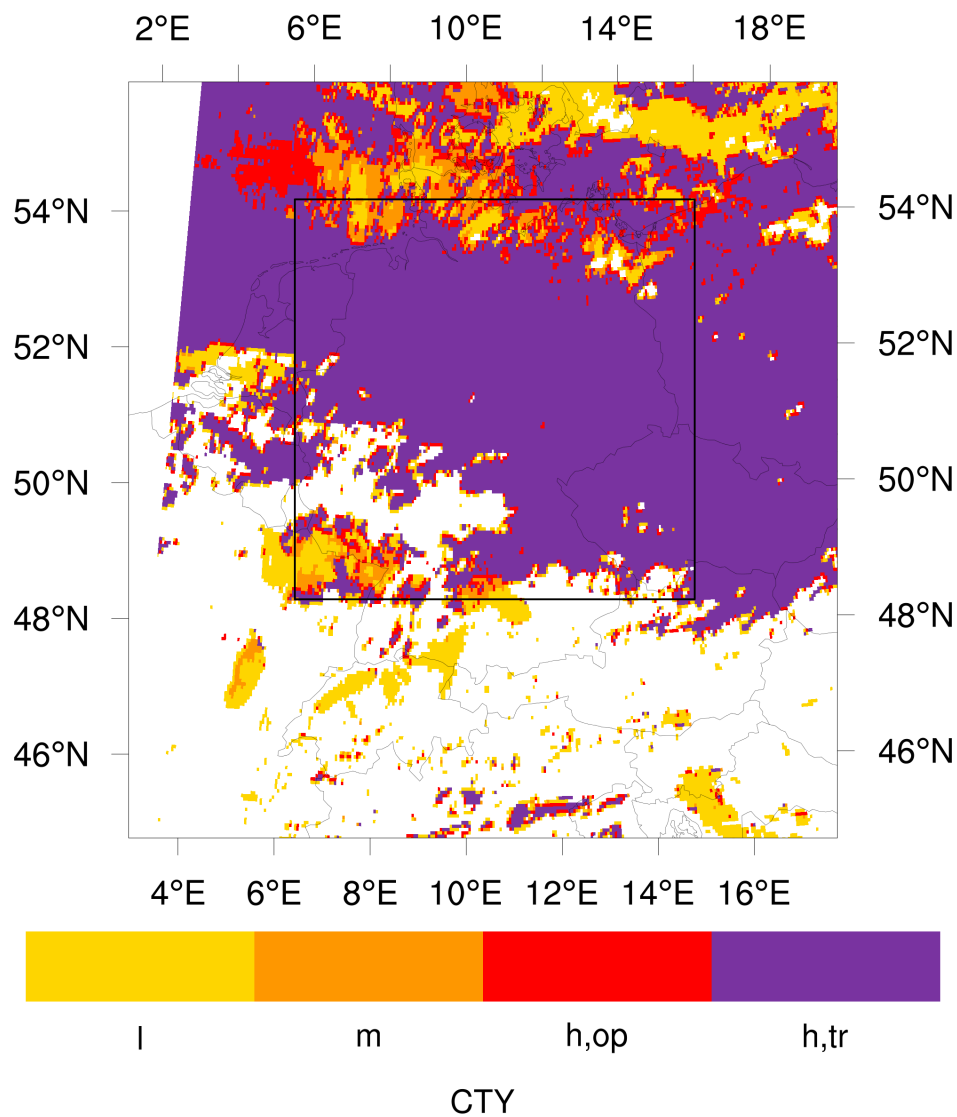
Figure 9. a) Cloud types (CM SAF) at 12 UTC 3 December 2013 with low (l), medium (m), high opaque (h,op) and high transparent (h,tr) clouds (for details see section 4.3).
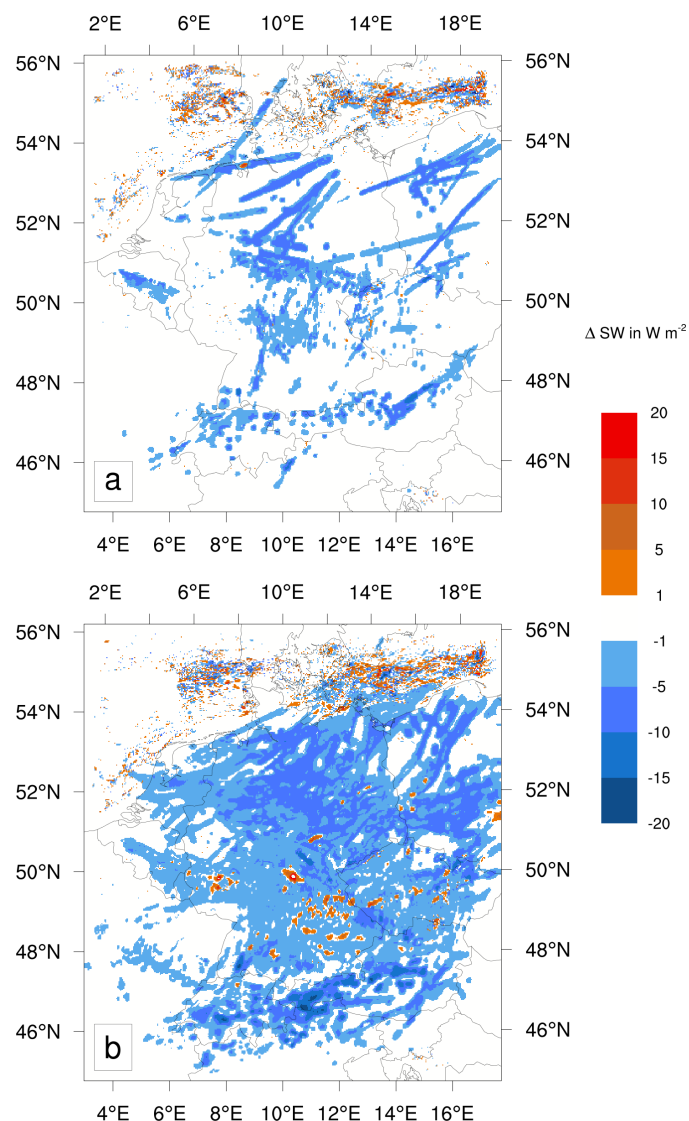
Figure 10. Difference in shortwave incoming radiation for aviation simulation and reference simulation for 3 December 2013 at the surface, a) 10 UTC, b) 12 UTC.

cirrus ice class. The case study for this particular day shows that the inclusion of aircraft effects in a regional weather forecast model improves the representation of high level clouds.

4.4   Contrail Impact on Surface Radiative Fluxes

Figure 10 shows the changes in the incoming shortwave radiation (SW) at two points in time at the surface. Clearly, additional

5   ice crystals caused by air traffic reduce the incoming SW radiation. The line-shaped structure of young contrails at 10 UTC
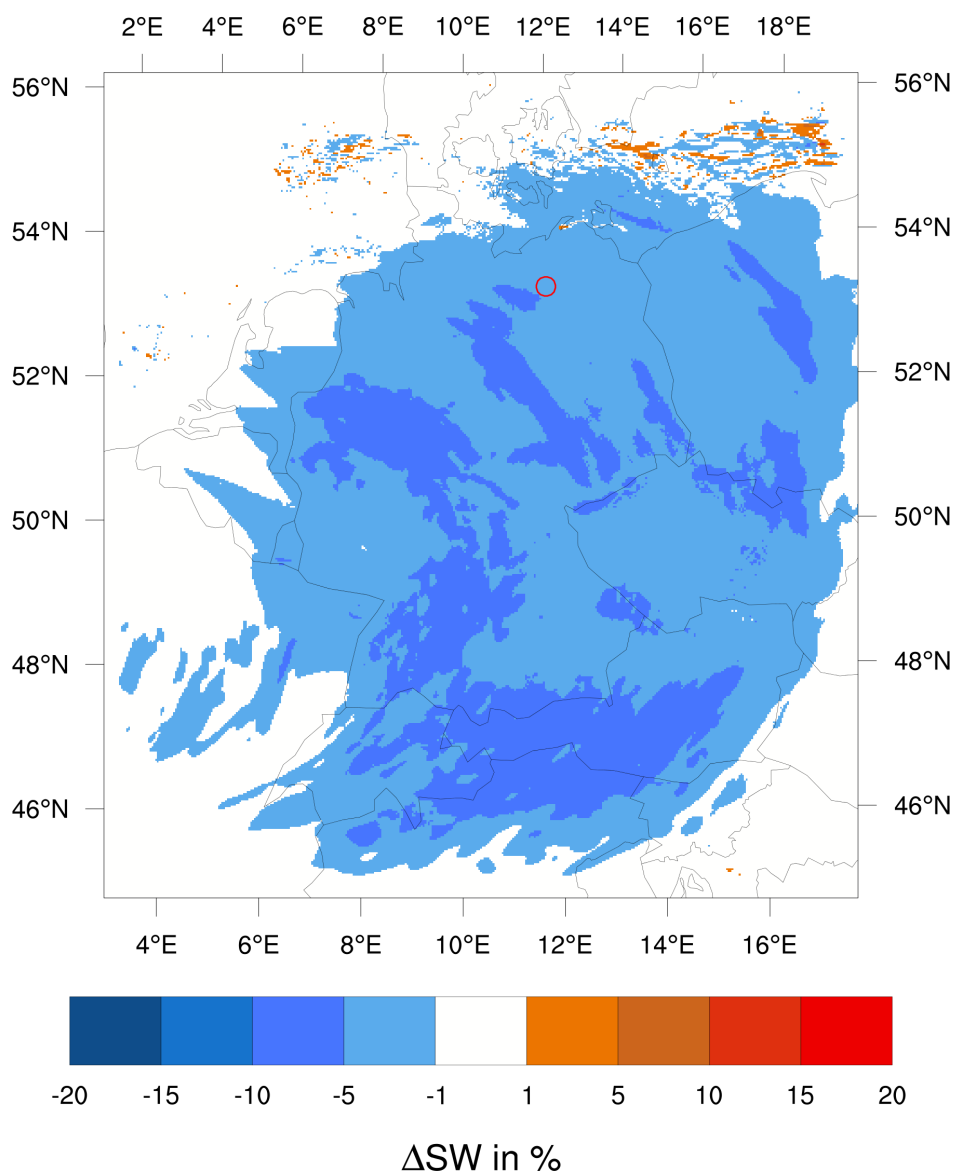
Figure 11. Average changes in the amount of incoming diffuse and direct solar radiation during daylight hours of 3 December 2013 at the surface (aviation simulation minus reference simulation). The red circle marks the location evaluated in Fig. 12.
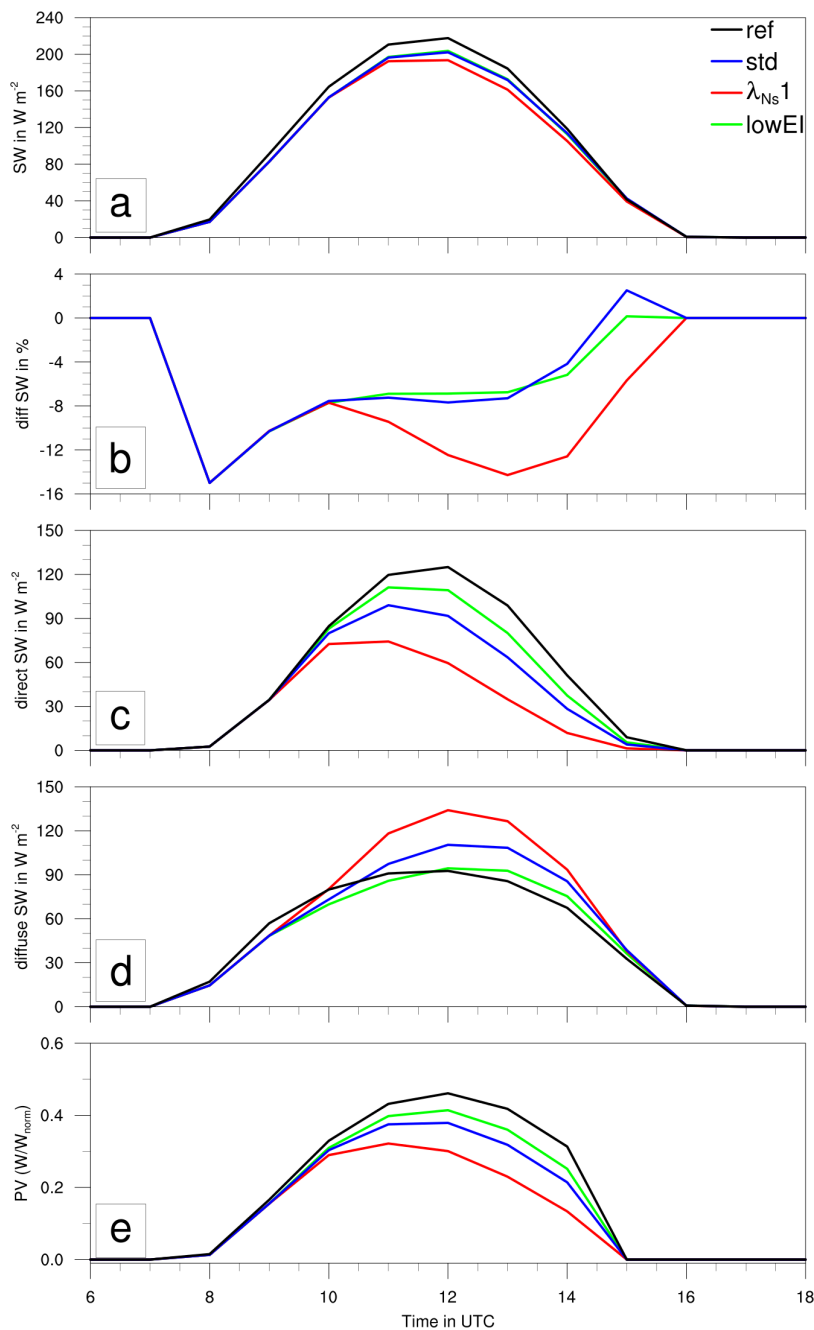
Figure 12. Temporal evolution for 3 December 2013 of incoming shortwave radiation: reference (black); aviation simulation as before (blue); "bio-fuel" scenario with $EI_{iceno} \times 0.1$ (green), omission of crystal loss during contrail vortex phase with $\lambda_{Ns} = 1$ (red): a) total; b) difference in total SW between aviation simulation and reference simulation c) direct; d) diffuse; e) normalized PV-power diffuse; all for the location marked with the red circle in Fig. 11.

(Fig. 3a) is reflected in similar patterns of reduced SW radiation (Fig. 10a). As disussed earlier, the contrail ice class features numerous very small ice crystals with a high extinction coefficient. In the case investigated, this leads to a reduction in incoming SW radiation of 1 to 15 Wm^{-2}. As previously mentioned, our parameterizations are not able to calculate the optical properties of ice crystals with effective radii below the threshold of 5 μm. Rather, crystals with an effective radius of less than 5 μm are

5   assumed to have optical properties of crystals as large as 5 μm. Therefore, the shading effect of the contrail ice crystals might be underestimated in our calculations.

A strong spatial increase in the shading effect is found at 12 UTC (Fig. 10b). Here, the contrail coverage reaches its maximum. Still partly line shaped contrails are found with a similar reducing impact as two hours before. Additionally, clusters of contrail ice transformed into the cirrus ice class have evolved, particularly over the center of the domain (Fig. 4b). The ice crystals

10   herein are relatively small, but larger than those present in the contrail ice class. Therefore, they inhibit less SW radiation from reaching the ground than the ice crystals in the contrail ice class. Consequently, the reduction on SW radiation here is smaller, but still reaches 1 to 10 Wm^{-2}.

Especially in the north of the domain, small areas with the difference in incoming SW radiation attaining large negative values adjacent to large positive values are found. They occur when subtracting e. g. fields of radiative fluxes of the aviation simulation

15   from those of the reference simulation. The introduction of contrail ice acts as source of disturbance for various processes like convection or turbulence. Those features are to be classified as noise as they do not influence the overall situation.

Non-negligible areas with an increase in SW radiation occur, e. g. at 12 UTC over the south-eastern part of the domain (Fig. 10b). Besides only reducing the direct incoming SW radiation, contrail ice crystals also enlarge the flux of diffuse SW radiation (see below). On occasion, as the simulated contrails are still rather optically thin, this effect may be larger than the

20   reduction of direct radiation.

The average change of incoming direct and diffuse SW for 3 December 2013 is shown in Fig. 11. Also here, the small scale fluctuating values in the north are most likely noise.

The thin veil of contrail cirrus that spreads over most of the domain causes an average decrease of incoming direct and diffuse SW radiation of 1 to 5 %. The large and persistent contrail cluster over the northern and eastern part of the domain inhibits on

25   average 5 to 10 % of SW radiation from reaching the ground during approximately eight hours of daylight. The reduction is strongest over the south and the west of the domain. Here, contrail ice is present for the longest time, as seen in Fig. 7.

Fig. 12a shows the temporal evolution of the total incoming SW radiation in an area of approximately 140 km × 140 km centered at a spot in the north-eastern part of the simulated domain, indicated by the red circle in Fig. 11. Around noon, between 10 UTC and 13 UTC, contrails and contrail cirrus reduce up to 20 Wm^{-2} of the incoming SW radiation (Fig. 12a).

30   This is a decrease of about 7 % (Fig. 12b). The effect is largest in the morning and ceases during the day. This corresponds to the size of contrail ice crystals. As in our simulation, contrails start to form at 8 UTC, the average contrail ice crystal size grows during the day. Accordingly, contrail ice effective radii also increase with time and lead to a smaller values of the extinction coefficient. At 15 UTC, the incoming SW radiation is larger in the aviation simulation compared to the reference simulation. This is caused by the diffusive share of incoming SW radiation that is enhanced in the aviation simulation. The strongest

35   reduction in the morning as well as the increase in SW radiation in the afternoon occur with very small total values of total SW

radiation, the effect therefore is negligible here.

Separating the total SW radiation into its direct (Fig. 12c) and diffuse (Fig. 12d) fraction, it is clear that especially the direct incoming SW radiation is strongly reduced by up to 30 Wm^{-2} due to the presence of additional ice crystals in the atmosphere. In contrast, the diffuse incoming SW radiation is increased by up to 20 Wm^{-2}. Enhanced scattering of SW radiation caused by

5 the contrail ice crystals increases the diffuse SW radiation at the ground. Between 8 UTC and about 10 UTC, the amount of diffuse SW radiation reaching the ground is larger in the aviation simulation. During this time, as mentioned before, contrail ice crystals are smallest on average and forward scattering is less pronounced than for larger crystals.

The overall picture indicates that young and aged contrails reduce the incoming SW radiation at the surface. This effect is currently neglected in operational weather forecast models. However, this effect is of relevance for the production of solar

10 energy. The temporal evolution of the normalized PV power is depicted in Fig. 12e. This quanitity is caluated using the open source PV modeling environment PV_LIB for python (Andrews et al., 2014). A nominal capacity is assumed, consisting of a specific PV module and PV inverter combination. The tilt and orientation of the PV module as well as the technical specifications are taken from Rieger et al. (2017). They assume panels consisting of a south-oriented PV module with a nominal power of 220W and a size of $1.7 \mathrm{m}^2$. Compared to the reference simulation, the normalized PV power is decreased

15 in the aviation simulation. The largest losses occur at noon and are up to 10 %. The normalized PV power is somewhat more strongly reduced than the total SW radiation. For production of PV power, the incoming direct radiation is of greater importance than the diffuse; of the two, the direct experiences the larger reduction from contrails and contrail cirrus.

4.5 Sensitivity to Initial Ice Crystal Number and Early Contrail Ice Crystal Loss

In this last section, we briefly examine two sensitivities of our model setup.

20 For the first, we reduce the emission index for ice crystals EI_{iceno} by a factor of 10 (green lines in Fig. 12). In reality, the usage of biofuels that cause lower soot concentrations when combusted, would have a similar effect (Moore et al., 2017). Due to this, the initial number concentration of contrail ice crystals is reduced, thus fewer but larger ice crystals are formed (Unterstrasser, 2014). In the simulation with reduced EI_{iceno}, the reduction of total incoming SW radiation is only slightly weaker than for the simulation assuming standard fuel (Fig. 12a, Fig. 12b). As ice crystals are slightly larger, their extinction coefficient is lower

25 and the reduction of direct SW radiation is smaller than for the standard setup (Fig. 12c). Also the increase in incoming diffuse SW radiation is less strong compared to the standard setup (Fig. 12d). Consequently, the reduction in normalized PV power is also less strong than for the standard setup (Fig. 12e).

Second, we set the surviving fraction of ice crystals λ_{Ns} in the parameterization of the initial ice crystal number to 1. This deliberately neglects the effects of crystal loss during the contrail vortex phase, as parametrized by Unterstrasser (2016). The

30 influence of this parameter is large. During daytime, a reduction in total incoming SW radiation of up to 15 % is simulated (Fig. 12a, Fig. 12b). Both the reduction in direct SW radiation as well as the increase in diffuse SW radiation are much more pronounced for this case (Fig. 12c, Fig. 12d). Especially the reduction in direct SW radiation causes a strong reduction in production of PV power. Here, losses of nearly 20 % occur at noon. When no early crystal loss is parametrized in the model, initial ice crystal number concentrations may be much higher than usual. As the initial IWC remains the same, the

new crystals are smaller and thus, the simulated contrails are optically thicker. The much stronger reduction in incoming SW radiation demonstrates that the early ice crystal number loss is non-negligible and an important aspect of contrail evolution as it has a long-lasting impact on contrail-cirrus radiative properties.

5 Conclusions

5 In this study, the regional atmospheric model COSMO-ART coupled with a two-moment microphysical scheme and a diagnostic treatment of radiation was extended by a parameterization describing contrails and the related physical processes. Methods for a separate but consistent treatment of contrail ice were implemented to satisfy the special requirements describing the microphysics in young contrails and the transition phase to contrail cirrus. It was shown how microphysical properties such as ice water content, ice crystal number concentration and the mean ice crystal radius of ice crystals in contrails change over

10 time and depend on the meteorological conditions. The ice water content in young contrails is comparable to that in thin cirrus clouds ranging from 0.2 to $5.0\,\mathrm{mg\,m^{-3}}$, but with considerably higher ice crystal number concentrations between $1\,\mathrm{cm^{-3}}$ and $100\,\mathrm{cm^{-3}}$ and effective radii below $10\,\mu\mathrm{m}$. The numerous small ice crystals produce high values for the extinction coefficient and thus also for the optical depth.

The transition of contrail ice into the cirrus ice class causes increasing number concentrations. Here, effective radius of the ice

15 crystals from the contrail ice class grows to an extent comparable to that of natural cirrus. Because of the still relatively high number concentrations, contrail cirrus still features high values for both the extinction coefficient and the optical depth.

Qualitative comparison with satellite data shows good agreement and proves advantages of considering contrails and contrail cirrus in a regional weather forecast model.

Contrail cirrus tends to cause changes in the microphysical appearance of high-level cloud coverage to a remarkable extent,

20 which in turn influences the radiative effect in these regions.

In addition, the impact of contrails and contrail cirrus on shortwave radiation and the production of PV power was quantified. Although the case study was performed for 3 December 2013, when solar zenith angles are low and the length of days is short, a strong influence of contrails is still simulated. They inhibit up to 5 to 10 % of shortwave radiation from reaching the ground at noon. This results in a loss of PV power production of up to 10 %.

25 Moreover, it was demonstrated that ice crystal loss in young contrails is an important process which can significantly change the contrail-cirrus properties on a regional scale. This study is the first approach to simulate contrails and contrail cirrus using a numerical weather prediction model with high spatial and temporal resolution. Subsequently, the presented method can serve as a basis for improving the predictability of the solar radiation in regional weather forecasting by taking into account contrails and contrail cirrus.

Appendix A: Ice microphysical model

This section expands the description of the microphysical model from section 2.1 and presents a collection of underlying equations. All formulae can be found in Seifert and Beheng (2006) as well. Values of constants used in this section are listed in Tab. 1. The generalized Γ-distribution is defined as

$$f(m) = A\, m^\nu \exp\left(-\lambda m^\mu\right) \tag{A1}$$

The parameters ν and μ are assumed constant, respectively. The parameter A is related to the total ice crystal number concentration $n = M^0$ and λ to the ice crystal mean mass $\overline{m} = q_i/n = M^1/M^0$. Expressions involving Γ-functions exist for the moments

$$M^k(A,\lambda) = \int_0^\infty m^k f(m; A,\lambda)\, dm \tag{A2}$$

of order k (not shown).

The growth equation of a single ice crystal is given by (Pruppacher and Klett, 1997):

$$\frac{dm}{dt} = \frac{4\pi C(m) F_{\mathrm{ven}}(m) S_i}{\frac{R_v T}{p_{\mathrm{sat,i}}(T) D_v} + \frac{L_{iv}}{K_T T}\left(\frac{L_{iv}}{R_v T} - 1\right)} = 4 L(m)\, G_{iv}(T,p)\, F_{\mathrm{ven}}(m)\, S_i \tag{A3}$$

Here, T is the temperature, p is the pressure, and $C = D/\pi$ denotes the capacity of hexagonal crystals (Harrington et al., 1995). S_i is the supersaturation with respect to ice, L_{iv} represents the latent heat of sublimation, $p_{\mathrm{sat,i}}$ denotes the saturation vapor pressure over ice, R_v is the specific gas constant for water vapor, K_T is the conductivity of heat, and D_v is the molecular diffusion coefficient of water vapor. The term F_{ven} accounts for ventilation effects and G_{iv} considers the diffusion of water vapor and the effect of latent heating:

$$G_{iv}(T,p) = \left[\frac{R_v T}{p_{\mathrm{sat,i}} D_v} + \frac{L_{iv}}{K_T T}\left(\frac{L_{iv}}{R_v T} - 1\right)\right]^{-1} \tag{A4}$$

Integration of Eq. A3 over the ice crystal mass spectrum yields the temporal derivative of the ice mass density q_i:

$$\frac{\partial q_i}{\partial t} = 4 G_{iv}(T,p)\, S_i \int_{m_{min}}^{m_{max}} D(m)\, F_{\mathrm{ven}}(m)\, f(m)\, dm \tag{A5}$$

Similar to the mass-size relation (Eq. 2), the terminal settling velocity v is approximated by a power law (Eq. A6) with coefficients a_{vel} and b_{vel}.

$$v(m) = a_{\text{vel}} m^{b_{\text{vel}}} \tag{A6}$$

Integrating $v(m)$ and $m\, v(m)$ over the ice crystal mass spectrum yields mean fall velocities $\overline{v}_{\text{k}}$ for the ice crystal number $(k=0)$ and mass (k=1), respectively:

$$\overline{v}_{\text{k}} = a_{\text{vel}} \frac{\Gamma\left(\frac{k+\nu+b_{\text{vel}}+1}{\mu}\right)}{\Gamma\left(\frac{k+\nu+1}{\mu}\right)} \left[\frac{\Gamma\left(\frac{\nu+1}{\mu}\right)}{\Gamma\left(\frac{\nu+2}{\mu}\right)}\right]^{b_{\text{vel}}} \overline{m}^{b_{\text{vel}}} \tag{A7}$$

5   Using relations relying on potential functions like Eqs. A6 and 2 is beneficial. Then integrals over the mass distribution can often be expressed in terms of moments which avoids employing more expensive numerical quadrature techniques. The contrail class uses a piecewise definition of the mass size relation. In this case, truncated moments have to be evaluated.

     In the model, both self-collection and collection between the individual classes of frozen hydrometeors are considered. Sink terms (not shown) are included in the prognostic equations of n. In case that two different hydrometeor classes are present,

10   where class A has a larger mean mass than class B, the ice crystals of class B are collected by those of class A. In addition to the number loss in class B, mass is transferred from class B to class A.

     The nucleation process for natural cirrus is not repeated here as ice crystal generation in the contrail class is quite different (see section 3.1)

Appendix B: Radiation related derivations

15   For hexagonal columns, the mass of a single ice crystal is given by

$$m = \rho_{\text{ice}} \frac{3\sqrt{3}}{8} D^2 L. \tag{B1}$$

Combining the latter equation with Eq. 2 yields

$$D = \sqrt{\frac{8a}{3\sqrt{3}\rho_{\text{ice}}}} L^{\frac{b-1}{2}} \tag{B2}$$

For distributions, the transformation property $f_L(L) = f(m(L))\frac{dm}{dL}$ holds. Using the mass-size relation and the definition of a

20   general Γ-distribution, it follows

$$f_L(L) = A \left(a\, L^b\right)^{\nu} \exp\left(-\lambda \left(a\, L^b\right)^{\mu}\right)\, a\, b\, L^{b-1} \tag{B3}$$

$f_L(L)$ also represents a generalized Γ-distribution with parameters:

$$A_L = A\, a^{\nu+1}\, b; \;\; \nu_L = b(\nu+1) - 1; \;\; \lambda_L = \lambda a^{\mu}; \;\; \mu_L = b\mu \tag{B4}$$

Plugging Eq. B2 into Eq. 3 and using the latter relations, the integrals in the effective radius definition can be re-formulated in terms of moments.

References

Andrews, R., Stein, J., Hansen, C., and Riley, D.: Introduction to the Open Source PV_LIB for Python Photovoltaic System Modelling Package, 40th IEEE Photovoltaic Specialist Conference, 2014.

Appleman, H.: The Formation of Exhaust Condensation Trails by Jet Aircraft., Bull. Am. Meteorol. Soc., 34, 14 – 20, 1953.

5   Baldauf, M., Seifert, A., Forstner, J., Majewski, D., Raschendorfer, M., and Reinhardt, T.: Operational convective-scale numerical weather prediction with the COSMO model: description and sensitivities, Mon. Wea. Rev., 139, 3887 – 3905, doi:10.1175/MWR-D-10-05013.1, 2011.

Bock, L. and Burkhardt, U.: The temporal evolution of a long-lived contrail cirrus cluster: Simulations with a global climate model, J. Geophys. Res. Atmos., 121, doi:10.1002/2015JD024475, 2016.

10   Boucher, O., Randall, D., Artaxo, P., Bretherton, C., Feingold, G., Forster, P., Kerminen, V.-M., Kondo, Y., Liao, H., Lohmann, U., Rasch, P., Satheesh, S., Sherwood, S., Stevens, B., and Zhang, X.: Clouds and Aerosols. In: T.F. Stocker, D. Qin, G.-K. Plattner, M. Tignor, S.K. Allen, J. Boschung, A. Nauels, Y. Xia, V. Bex, P.M. Midgley (eds.), Climate Change 2013: The Physical Science Basis (Contribution of Working Group I to the Fifth Assessment Report of the Intergovernmental Panel on Climate Change), Cambridge University Press, Cambridge, United Kingdom and New York, NY, USA, 2013.

15   Burkhardt, U. and Kärcher, B.: Process-based simulation of contrail cirrus in a global climate model, J. Geophys. Res., 114, D16 201, doi:10.1029/2008JD011491, 2009.

Burkhardt, U. and Kärcher, B.: Global radiative forcing from contrail cirrus, Nat. Clim. Change, 1, 54 – 58, doi:10.1038/NCLIMATE1068, 2011.

DLR: ftp://taurus.caf.dlr.de/put/wetterbilder/, 01.01.2014, ftp://taurus.caf.dlr.de/put/wetterbilder/, 2014.

20   Eleftheratos, K., Zerefos, C., Zanis, P., Balis, D., Tselioudis, G., Gierens, K., and Sausen, R.: A study on natural and manmade global interannual fluctuations of cirrus cloud cover for the period 1984-2004, Atmos. Chem. Phys., 7, 2631 – 2642, doi:10.5194/acp-7-2631-2007, 2007.

Febvre, G., Gayet, J. F., Minikin, A., Schlager, H., Shcherbakov, V., Jourdan, O., Busen, R., Fiebig, M., Kärcher, B., and Schumann, U.: On optical and microphysical characteristics of contrails and cirrus, J. Geophys. Res., 114, D02 204, doi:10.1029/2008JD01018, 2009.

25   flightradar24.com: http://www.flightradar24.com, 16.08.2015, http://www.flightradar24.com, 2015.

Freudenthaler, V., Homburg, F., and Jäger, H.: Contrail observations by ground-based scanning lidar: Cross-sectional growth, Geophys. Res. Lett., 22, 3501–3504, 1995.

Fu, Q., Yang, P., and Sun, W.: An Accurate Parameterization of the Infrared Radiative Properties of Cirrus Clouds for Climate Models, J. Clim., 11, 2223 – 2237, 1998.

30   Harrington, J., Meyers, M., Walko, R., and Cotton, W.: Parameterization of ice crystal conversion processes due to vapor deposition for mesoscale models using doublemoment basis functions. Part I: Basic formulation and parcel model results, J. Atmos. Sci., 52, 4344 – 4366, 1995.

Heymsfield, A. and Iaquinta, J.: Cirrus crystal terminal velocities, J. Atmos. Sci., 57, 916–938, 2000.

Heymsfield, A., Baumgardner, D., DeMott, P., Forster, P., Gierens, K., and Kärcher, B.: Contrail Microphysics, Bull. Am. Meteorol. Soc.,

35   91, 465 – 472, doi:10.1175/2009BAMS2839.1., 2010.

Kärcher, B., Burkhardt, U., Bier, A., Bock, L., and Ford, I.: The microphysical pathway to contrail formation, J. Geophys. Res. Atmos., 120, 7893–7927, doi:10.1002/2015JD023491, 2015.

Key, J. R., Yang, P., Baum, B. A., and Nasiri, S. L.: Parameterization of shortwave ice cloud optical properties for various particle habits, J. Geophys. Res. Atmos., 107, AAC 7–1–AAC 7–10, doi:10.1029/2001JD000742, 2002.

Khou, J.-C., Ghedhaïfi, W., Vancassel, X., and Garnier, F.: Spatial Simulation of Contrail Formation in Near-Field of Commercial Aircraft, J. Aircraft, 52, 1927–1938, doi:10.2514/1.C033101, http://dx.doi.org/10.2514/1.C033101, 2015.

5 Lewellen, D. and Lewellen, W.: The effects of aircraft wake dynamics on contrail development, J. Atmos. Sci., 58, 390 – 406, 2001.

Lewellen, D., Meza, O., and Huebsch, W.: Persistent Contrails and Contrail Cirrus. Part I: Large-Eddy Simulations from Inception to Demise, J. Atmos. Sci., 71, 4399 – 4419, doi:10.1175/JAS-D-13-0316.1., 2014.

Lewellen, D. C.: Persistent contrails and contrail cirrus. Part 2: Full Lifetime Behavior, J. Atmos. Sci., pp. 4420–4438, doi:10.1175/JAS-D-13-0317.1, 2014.

10 Marquart, S., Ponater, M., Mager, F., and Sausen, R.: Future development of contrail cover, optical depth and radiative forcing: Impacts of increasing air traffic and climate change, J. Clim., 16, 2890 – 2904, 2003.

Minnis, P., Ponater, M., Young, D. F., Garber, D. P., Nguyen, L., Jr, W. L. S., and Palikonda, R.: Transformation of Contrails into Cirrus during SUCCESS, Geophys. Res. Lett., 25, 1157 – 1160, 1998.

Moore, R. H., Thornhill, K. L., Weinzierl, B., Sauer, D., D'Ascoli, E., Kim, J., Lichtenstern, M., Scheibe, M., Beaton, B., Beyersdorf, A. J.,
15   Barrick, J., Bulzan, D., Corr, C. A., Crosbie, E., Jurkat, T., Martin, R., Riddick, D., Shook, M., Slover, G., Voigt, C., White, R., Winstead, E., Yasky, R., Ziemba, L. D., Brown, A., Schlager, H., and Anderson, B. E.: Biofuel blending reduces particle emissions from aircraft engines at cruise conditions, Nature, 543, 411–415, http://dx.doi.org/10.1038/nature21420, 2017.

Paoli, R., Nybelen, L., Picot, J., and Cariolle, D.: Effects of jet/vortex interaction on contrail formation in supersaturated conditions, Phys. Fluids, 25, 1–28, doi:10.1063/1.4807063, 2013.

20 Ponater, M., Marquart, S., and Sausen, R.: Contrails in a comprehensive global climate model: Parameterization and radiative forcing results, J. Geophys. Res. Atmos., 107, 941 – 960, doi:10.1029/2001JD000429, 2002.

Pruppacher, H. R. and Klett, J. D.: Microphysics of clouds and precipitation, Dordrecht: Kluwer Academic Publishers, 1997.

Rieger, D., Steiner, A., Bachmann, V., Gasch, P., Förstner, J., Deetz, K., Vogel, B., and Vogel, H.: Impact of the 4 April 2014 Saharan dust outbreak on the photovoltaic power generation in Germany, Atmos. Chem. Phys. Discuss., https://doi.org/10.5194/acp-2017-441, 2017.

25 Ritter, B. and Geleyn, J.-F.: A comprehensive radiation scheme for numerical weather prediction models with potential applications in climate simulations, Mon. Wea. Rev., 120, 303 – 325, 1992.

Sausen, R., Isaksen, I., Grewe, V., Hauglustaine, D., Lee, D., Myhre, G., Köhler, M., Pitari, G., Schumann, U., and et al., F. S.: Aviation radiative forcing in 2000: An update on IPCC (1999), Meteorol. Z., 14, 555 – 561, doi:10.1127/0941-2948/2005/0049, 2005.

Schmidt, E.: Die Entstehung von Eisnebel aus den Auspuffgasen von Flugmotoren, Schriften der Deutschen Akademie der Luftfahrt-
30   forschung, 44, 1 – 15, 1941.

Schröder, F., Kärcher, B., Duroure, C., Ström, J., Petzold, A., Gayet, J.-F., Strauss, B., Wendling, P., and Borrmann, S.: On the Transition of Contrails into Cirrus Clouds, J. Atmos. Sci., 57, 464 – 480, 2000.

Schulz, J., Albert, P., Behr, H.-D., Caprion, D., Deneke, H., Dewitte, S., Dürr, B., Fuchs, P., Gratzki, A., Hechler, P., Hollmann, R., Johnston, S., Karlsson, K.-G., Manninen, T., Nüller, R., Reuter, M., Riihelä, A., Roebeling, R., Selbach, N., Tetzlaff, A., Thomas, W., Werscheck,
35   M., Wolters, E., and Zelenka, A.: Operational climate monitoring from space: the EUMETSAT Satellite Application Facility on Climate Monitoring (CM-SAF), Atmos. Chem. Phys., 9, 1687 – 1709, doi:10.5194/acp-9-1687-2009, 2009.

Schumann, U.: On conditions for contrail formation from aircraft exhausts, Meteorol. Z., 5, 4 – 23, 1996.

Schumann, U.: A contrail cirrus prediction model, Geosci. Model Dev., 5, 543–580, doi:10.5194/gmd-5-543-2012, 2012.

Schumann, U. and Graf, K.: Aviation-induced cirrus and radiation changes at diurnal timescales, J. Geophys. Res. Atmos., 118, 2404–2421, doi:10.1002/jgrd.50184, 2013.

Seifert, A. and Beheng, K. D.: A two-moment cloud microphysics parameterization for mixed-phase clouds. Part 1: Model description, Meteorol. Atmos. Phys., 92, 45 – 66, doi:10.1007/s00703-005-0112-4, 2006.

5   Spichtinger, P. and Gierens, K. M.: Modelling of cirrus clouds - Part 1a: Model description and validation, Atmos. Chem. Phys., 9, 685–706, 2009.

Stubenrauch, C. and Schumann, U.: Impact of air traffic on cirrus coverage, Geophys. Res. Lett., 32, doi:10.1029/2005GL022707, 2005.

Unterstrasser, S.: Large-eddy simulation study of contrail microphysics and geometry during the vortex phase and consequences on contrail-to-cirrus transition, J. Geophys. Res. Atmos., 119, 7537–7555, doi:10.1002/2013JD021418, 2014.

10 Unterstrasser, S.: Properties of young contrails - a parametrisation based on large - eddy simulations, Atmos. Chem. Phys., 16, 2059 – 2082, doi:10.5194/acp-16-2059-2016, 2016.

Unterstrasser, S. and Gierens, K.: Numerical simulations of contrail-to-cirrus transition - Part 1: An extensive parametric study, Atmos. Chem. Phys., 10, 2017–2036, 2010a.

Unterstrasser, S. and Gierens, K.: Numerical simulations of contrail-to-cirrus transition - Part 2: Impact of initial ice crystal number, radiation,
15   stratification, secondary nucleation and layer depth, Atmos. Chem. Phys., 10, 2037–2051, 2010b.

Unterstrasser, S. and Görsch, N.: Aircraft-type dependency of contrail evolution, J. Geophys. Res. Atmos., 119, 14,015–14,027, doi:10.1002/2014JD022642, 2014JD022642, 2014.

Unterstrasser, S., Gierens, K., Sölch, I., and Lainer, M.: Numerical simulations of homogeneously nucleated natural cirrus and contrail-cirrus. Part 1: How different are they?, Meteor. Z., doi:10.1127/metz/2016/0777, http://dx.doi.org/10.1127/metz/2016/0777, 2016a.

20 Unterstrasser, S., Gierens, K., Sölch, I., and Wirth, M.: Numerical simulations of homogeneously nucleated natural cirrus and contrail-cirrus. Part 2: Interaction on local scale, Meteor. Z., doi:10.1127/metz/2016/0780, http://dx.doi.org/10.1127/metz/2016/0780, 2016b.

Vogel, B., Vogel, H., Bäumer, D., Bangert, M., Lundgren, K., Rinke, R., and Stanelle, T.: The comprehensive model system COSMO-ART - Radiative impact of aerosol on the state of the atmosphere on the regional scale, Atmos. Chem. Phys., 9, 8661 – 8680, doi:10.5194/acpd-9-14483-2009, 2009.

25 Voigt, C., Schumann, U., Jurkat, T., Schäuble, D., Schlager, H., Petzold, A., Gayet, J.-F., Krämer, M., Schneider, J., Borrmann, S., Schmale, J., Jessberger, P., Hamburger, T., Lichtenstern, M., Scheibe, M., Gourbeyre, C., Meyer, J., Kübbeler, M., Frey, W., Kalesse, H., Butler, T., Lawrence, M. G., Holzäpfel, F., Arnold, F., Wendisch, M., Döpelheuer, A., Gottschaldt, K., Baumann, R., Zöger, M., Sölch, I., Rautenhaus, M., and Dörnbrack, A.: In-situ observations of young contrails – overview and selected results from the CONCERT campaign, Atmos. Chem. Phys., 10, 9039–9056, doi:10.5194/acp-10-9039-2010, 2010.

Table 1. Microphysical constants of microphysical model. If different values are used for the natural and the contrail ice class, the subscripts con and nat are added.

Symbol	Definition	Value	Reference
$m_{\mathrm{max,con}}$	maximum $\overline{m}$	2×10^{-11} kg	this study
$m_{\mathrm{min,con}}$	minimum $\overline{m}$	10^{-15} kg	this study
$m_{\mathrm{max,nat}}$	maximum $\overline{m}$	10^{-6} kg	Seifert and Beheng (2006)
$m_{\mathrm{min,nat}}$	minimum $\overline{m}$	10^{-12} kg	Seifert and Beheng (2006)
μ	parameter of size distribution	0.333	Seifert and Beheng (2006)
ν	parameter of size distribution	1	Seifert and Beheng (2006)
$a_{\mathrm{geo,con}}$	parameter in mass-size relation	526.1 and 0.04142	Spichtinger and Gierens (2009); Heymsfield and Iaquinta (2000)
$b_{\mathrm{geo,con}}$	exponent in mass-size relation	3 and 2.2	Spichtinger and Gierens (2009); Heymsfield and Iaquinta (2000)
$a_{\mathrm{geo,nat}}$	parameter in mass-size relation	1.59	A. Seifert, personal communication, June, 01, 2017
$b_{\mathrm{geo,nat}}$	exponent in mass-size relation	2.56	A. Seifert, personal communication, June, 01, 2017
a_{vel}	parameter in fallspeed relation	317.0 m s^{-1} g$^{b_{\mathrm{vel}}}$	Seifert and Beheng (2006)
b_{vel}	parameter in fallspeed relation	0.363	Seifert and Beheng (2006)
$L_{\mathrm{max,con}}$	crystal size corresponding to $m_{\mathrm{max,con}}$	58 µm	-
$L_{\mathrm{min,con}}$	crystal size corresponding to $m_{\mathrm{min,con}}$	1.24 µm	-
$L_{\mathrm{max,nat}}$	crystal size corresponding to $m_{\mathrm{max,nat}}$	3800 µm	-
$L_{\mathrm{min,nat}}$	crystal size corresponding to $m_{\mathrm{min,nat}}$	17.5 µm	-

Symbol	Definition	Unit
Γ	gamma function	-
λ, λ_L	slope parameter of generalized Γ-distribution	kg$^{-\mu}$, m$^{-\mu}$
λ_{Ns}	surviving fraction of ice crystals	-
μ	parameter of generalized Γ-distribution	-
ν	parameter of generalized Γ-distribution	-
ρ, ρ_{ice}	air density, density of ice	kg m^{-3}
A, A_L	scaling parameter of generalized Γ-distribution	m^{-3} kg^{-1}, m^{-4}
a_{geo}, a_{nat}	parameter in mass-size relation	-
a_{vel}	parameter in fallspeed relation	m s^{-1}kg$^{-b_{vel}}$
b_{con}, b_{nat}	exponent in mass-size relation	-
b_{vel}	exponent in fallspeed relation	-
c_p	specific heat capacity of air	J kg^{-1} K^{-1}
C	capacity	-
CTY	cloud type	-
d	flight distance	m
D_v	molecular diffusion coefficient	m
E	extinction coefficient	m^{-1}
E_{AB}	collision efficiency for classes A and B	-
EI_{iceno}	emission index for ice crystals	kg^{-1}
f, f_L	number concentration size distribution	m^{-3} kg^{-1}, m^{-3} m^{-1}
F_{ven}	ventilation coefficient	-
I	ice mass mixing ratio	kg kg^{-1}
q_{init}	"emitted" ice crystal mass concentration	kg m^{-3}
I_0	water vapor emission per flight distance	kg m^{-1}
q_i	ice crystal mass concentration	kg m^{-3}
K_T	conductivity of heat	J m^{-1}s^{-1}K^{-1}
L	ice crystal size	m
L_{iv}	latent heat for sublimation	J kg^{-1}
L_{max}	maximum particle length	m
L_{min}	minimum particle length	m
M^k	k^{th} power moment of $f(x)$	kg^k m^{-3}
n	ice crystal number concentration	m^{-3}
N	number concentration	kg^{-1}
N_{BV}	Brunt-Väisälä frequency	s^{-1}

n_{init}	"emitted" ice crystal number concentration	m^{-3}
N_s	number of surviving ice crystals per flight distance	m^{-1}
N_0	number of produced ice crystals per flight distance	m^{-1}
p	pressure	hPa
p_{sat}	saturation pressure	hPa
r	radius	μ m
r_e	effective radius	μ m
R_d	specific gas constant for dry air	J kg^{-1} K^{-1}
R_v	specific gas constant for water vapor	J kg^{-1} K^{-1}
RH_i	relative humidity with respect to ice	-
S_i	supersaturation with respect to ice	-
t	time	s
T	temperature	kg
v	velocity	m s^{-1}
V	volume	m^3
b_{span}	wing span	m